
Article:
Chen, H., Chen, Z. and Li, Y. orcid.org/0000-0001-7907-5176 (2020) Modulation of the secondary Bjerknes force in multi-bubble systems. Ultrasonics Sonochemistry, 61. ISSN 1350-4177

https://doi.org/10.1016/j.ultsonch.2019.104814

Modulation of the secondary Bjerknes force in multi-bubble systems

Haiyan Chen, Ziliang Chen

School of Material and Energy, Guangdong University of Technology, Guangzhou, China, 510006

Yi Li*

School of Mathematics and Statistics, University of Sheffield, Sheffield, UK, S3 7RH

Abstract

The behaviours of insonated bubble clusters are regulated by the secondary Bjerknes force between bubble pairs. While the force has been investigated extensively for two-bubble systems, the modulation of the force by nearby bubbles remains unclear. This problem is investigated in this paper by theoretical analyses and numerical simulations of a three bubble system. For weak oscillations, the third bubble is found to have strong effects when its radius is close to the resonant radius. The equilibrium distance between the bubble pair is reduced when the radius of the third bubble is smaller than the resonant threshold, and increased when it is larger. For strong oscillations of bubbles with radii of a few microns, the third bubble reduces the magnitude of the force, hence increasing the equilibrium distance. The modulation effects depend strongly on the relative sizes of the bubbles. Stronger effects can be produced when the third bubble is placed closer to the smaller bubble in the bubble pair. The findings highlight the need for a more accurate parametrization of the secondary Bjerknes force in the simulation and manipulation of bubble clusters.

Keywords: Bubble clusters, secondary Bjerknes force, linear analysis, numerical simulations

1. Introduction

When two bubbles are oscillating in a acoustically driven fluid, they experience an inter-bubble force, the secondary Bjerknes force [20, 5]. Bjerknes [4] shows that the force is attractive (repulsive) when the two bubbles oscillate in (out of) phase (see also [8]). This theory, however, does not account for the change of the force with the distance between the bubbles. Linear theories [32] predict that the force may become repulsive when the distance is small even if the force is initially attractive, thus suggest a possible stable distance between the two bubbles. This prediction provide a possible explanation for the formation of stable bubble clusters [20, 5, 24, 22, 19]. The sign change has been observed experimentally in, e.g., [31]. The detailed behaviours of the force can be modified by other physical processes, such as the multiple scattering effect, nonlinear resonance, shape oscillations, the coupling with the translation of the bubbles, and multi-frequency driving [28, 29, 12, 23, 2, 14, 27, 31, 16, 33].

Bubble clusters or bubble clouds are observed in biomedicine, metallurgical industries, food processing, and other applications (see, e.g., [6, 3, 30, 13]). There is a strong interest in the modelling and simulations of bubble clusters. The evolution of bubble clusters is regulated by the secondary Bjerknes force between the bubbles. Simplified models for the force have been adopted in the simulations of bubble clusters [24, 26, 22] using the particle method. The particle method is simple and versatile in that it can handle clusters with a wide range of different bubbles. It has been combined with continuum models in recent research (see, e.g., [21]). In this method, the individual bubbles are described by the equation of motion, of which the secondary Bjerknes force is an important component. In previous research [26, 24], the parameters calculated from isolated two-bubble systems have been used to model the force. The modulation of the force by surrounding bubbles has been ignored. In other applications, the secondary Bjerknes force has been used to manipulate bubbles as carriers of micro-devices [15, 18, 1]. When the manipulation is carried out for multiple bubbles, the modulation effects of additional bubbles will again need to be considered. To address this question, a coupled three-bubble system is analyzed theoretically and numerically. The dependence of the secondary Bjerknes force between two bubbles is calculated for different parameters. The equilibrium distance between the two bubbles, as a characteristic of the

*To whom correspondence should be addressed.
Email address: yili@sheffield.ac.uk. (Yi Li)

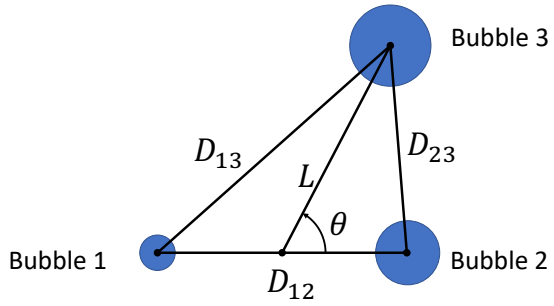

Figure 1: The illustration of the three bubble system. L is the distance from the third bubble to the mid-point of the line joining the centers of bubble 1 and 2. The radii of the bubbles in the figure do not correspond to those used in the calculation.

force, are documented. The results show that the behaviour of the secondary Bjerknes force can be altered significantly in a non-trivial way, which call for additional efforts in the modelling of the secondary Bjerknes force in bubble clusters.

The paper is organized as follows: the dynamical equations for the bubbles are explained in Section 2. Numerical simulations and a linear analysis of weak oscillations are presented in Section 3. Simulations of strong oscillations are discussed in Section 4. The conclusions are summarized in Section 5.

2. The governing equations

A system of $N = 3$ bubbles is considered in this investigation, which is illustrated in Fig. 1. $D_{ij} \equiv D_{ji}$ is the distance between bubble i and j. We also use L and θ as defined in the figure. The radius of bubble i is denoted by $R_i(t)$ and its equilibrium radius is R_{Ei}. Although the system appears to be highly simplified, the analysis of the system can be easily generalize to systems containing bubble clusters, by incorporating the cluster models in, e.g., [25].

It is assumed that the three bubbles are oscillating in a fluid with density ρ, surface tension σ and kinematic viscosity ν. The bubbles are driven by a harmonic uniform pressure with angular frequency ω:

$$p_I(t) = p_0 - p_a \sin(\omega t) \tag{1}$$

where p_0 is the ambient pressure and p_a is the amplitude of the ultrasonic pressure. Thus, we implicitly assume that, either the distances between the bubbles are small compared with the wave length of the pressure wave, or the bubbles reside on a plane of constant phase. The radii of the bubbles can be described by the Keller-Miksis model [17, 5] with additional pressure coupling terms between the bubbles. If the time-delay effects due to the finite propagation speed of the pressure wave are neglected, the coupling pressure between bubbles i and j, denoted as p_{ij}, is given by [23]

$$p_{ij}(t) = \frac{\rho}{D_{ij}} \frac{dR_j^2 \dot{R}_j}{dt}, \tag{2}$$

which is valid when the radii R_i and R_j are much smaller than D_{ij}. With p_{ij} included, the equation for $R_i(t)$ becomes [23]:

$$\begin{aligned} &2\rho(1 - c^{-1}\dot{R}_i)R_i\ddot{R}_i + \rho(3 - c^{-1}\dot{R}_i)\dot{R}_i^2 \\ =&2(1 + c^{-1}\dot{R}_i)(p_{wi} - p_I) + 2c^{-1}R_i(\dot{p}_{wi} - \dot{p}_I) \\ &- 2\rho \sum_{j=1}^{N'} D_{ij}^{-1}(2R_j\dot{R}_j^2 + R_j^2\ddot{R}_j), \end{aligned} \tag{3}$$

where

$$p_{wi} = \left(p_0 + \frac{2\sigma}{R_{Ei}}\right)\left(\frac{R_{Ei}}{R_i}\right)^{3k} - \frac{2\sigma}{R_i} - \frac{4\rho\nu\dot{R}_i}{R_i}, \tag{4}$$

is the pressure on the outer interface of bubble i, k is the polytropic exponent, and the summation $\sum_{j=1}^{N'}$ implies summing from $j = 1$ to $j = N$ excluding the $j = i$ term.

The pressure wave travels with a finite speed c, so the time for the pressure to propagate from bubble i to j is D_{ij}/c. If this time-delay effect is taken into account in the pressure coupling term, [7] shows that Eq. (3) becomes

$$\begin{aligned} &R_i\ddot{R}_i + \frac{3}{2}\dot{R}_i^2 + \sum_{j=1}^{N'} \frac{1}{D_{ij}} \frac{dR_j^2\dot{R}_j}{dt} \\ =&\frac{p_{wi} - p_I}{\rho} + \frac{1}{2c}\sum_{j=1}^{N} \frac{dR_j\dot{R}_j^2}{dt} \\ &+ \frac{1}{\rho c}\sum_{j=1}^{N} \frac{d(p_{wj} - p_I)R_j}{dt}. \end{aligned} \tag{5}$$

Note that the two summations on the right hand side include every term from $j = 1$ to N. Eq. (5) was given in a slightly different form in [7]. Eq. (5) is the model for the three bubble system we will be using in this paper. For the modelling of the time delay effect, see also [11].

Let F_{ij} denote the secondary Bjerknes force on bubble i induced by bubble j ($i \neq j$) [4, 8, 23]. By definition, F_{ij} is the time-averaged pressure force on bubble i generated by the oscillations of bubble j. As is explained in [7], the time-delay effect introduces an additional force on each bubble, but the forces do not contribute to the relative motion of the two bubbles. Therefore the time-delay effect on F_{ij} can be neglected. As a consequence, F_{ij} can be written as (see, e.g., [8]):

$$F_{ij} = \left\langle V_i \left.\frac{\partial p_j}{\partial r}\right|_{D_{ij}} \right\rangle = -\frac{\rho}{D_{ij}^2}\left\langle V_i \frac{dR_j^2\dot{R}_j}{dt}\right\rangle = \frac{\rho\langle \dot{V}_i\dot{V}_j\rangle}{4\pi D_{ij}^2}, \tag{6}$$

where V_i is the volume of bubble i and r is the radial distance from the center of bubble j. The pointed brackets represent averaging over a period of the driving pressure. F_{ij} is positive when it is attractive. It is obvious that F_{ij} is symmetric, i.e., $F_{ij} = F_{ji}$.

In a multiple-bubble system, F_{ij} is expected to depend not only on bubbles i and j but also the other bubbles. Nevertheless, in some previous bubble cluster simulations [24, 26], the calculation of F_{ij} has been simplified, where the factor $\langle \dot{V}_i \dot{V}_j \rangle$ is calculated from 2-bubble systems neglecting the contributions from other bubbles.

In terms of F_{ij}, the secondary Bjerknes force factor f_{ij} (see, e.g., [23]) is defined as

$$f_{ij} \equiv \rho \frac{\langle \dot{V}_i \dot{V}_j \rangle}{4\pi} \equiv D_{ij}^2 F_{ij}. \tag{7}$$

In this paper, the focus is on the effects of bubble 3 on F_{12} and f_{12}.

3. The analysis of weak oscillations

The modulation effects are first investigated analytically for small spherical oscillations to depict the possible scenarios. In this case, the compressibility and time-delay effects may be neglected. Let $R_i(t) = R_{Ei} + x_i(t)$ where R_{Ei} is the equilibrium radius of bubble i and $x_i(t) \ll R_{Ei}$ is the amplitude of the oscillations of bubble i. The linearized equation for x_i is thus

$$\ddot{x}_i + \frac{4\nu}{R_{Ei}^2}\dot{x}_i + \omega_i^2 x + \sum_{j=1}^{N'} \frac{R_{Ej}}{D_{ij}} \ddot{x}_j = \frac{p_a}{\rho R_{Ei}} \sin \omega t, \tag{8}$$

where

$$\omega_i \equiv \left[\frac{3kp_0}{\rho} + \frac{(3k-1)2\sigma}{\rho R_{Ei}} \right]^{1/2} \frac{1}{R_{Ei}}, \tag{9}$$

is the Minnaert frequency of bubble i [5].

We consider the inviscid case in what follows. It is sufficient to illustrate the calculation without cumbersome algebra. Assuming that there is no resonance ($\omega_i \neq \omega$), the stationary solution for $x_i(t)$ can be written as $x_i = \Re(A_i e^{i\omega t})$, where A_i is the complex amplitude and $\Re$ denotes taking the real part. Let $p_a \sin(\omega t) = \rho \Re(A_p e^{i\omega t})$, one finds from Eq. (8) that

$$M \begin{pmatrix} A_1 \\ A_2 \\ A_3 \end{pmatrix} = \begin{pmatrix} A_p \\ A_p \\ A_p \end{pmatrix}, \tag{10}$$

where the coefficient matrix M is given by

$$\begin{pmatrix} (\omega_1^2 - \omega^2)R_{E1} & -\frac{\omega^2 R_{E2}^2}{D_{12}} & -\frac{\omega^2 R_{E3}^2}{D_{13}} \\ -\frac{\omega^2 R_{E1}^2}{D_{21}} & (\omega_2^2 - \omega^2)R_{E2} & -\frac{\omega^2 R_{E3}^2}{D_{23}} \\ -\frac{\omega^2 R_{E1}^2}{D_{31}} & -\frac{\omega^2 R_{E2}^2}{D_{32}} & (\omega_3^2 - \omega^2)R_{E3} \end{pmatrix}. \tag{11}$$

From Eq. (10), one finds that

$$A_1 = \frac{A_p}{R_{E1}\Delta} \left\{ (1+\alpha_1)\omega_2^2 + g_1\omega^2 \right\}, \tag{12}$$

$$A_2 = \frac{A_p}{R_{E2}\Delta} \left\{ (1+\alpha_2)\omega_1^2 + g_2\omega^2 \right\}, \tag{13}$$

where

$$\begin{aligned} \Delta =& (\omega_1^2 - \omega^2 - \alpha_1\beta_1\omega^2)(\omega_2^2 - \omega^2 - \alpha_2\beta_2\omega^2) \\ & - \omega^4(\xi_1 + \alpha_2\beta_1)(\xi_2 + \alpha_1\beta_2), \end{aligned} \tag{14}$$

$$g_i = \xi_{3-i}(1+\alpha_{3-i}) - (1+\alpha_i) + (\alpha_i - \alpha_{3-i})\beta_{3-i}, \tag{15}$$

and

$$\xi_i = \frac{R_{Ei}}{D_{21}}, \quad \alpha_i = \frac{\omega^2 R_{E3}}{(\omega_3^2 - \omega^2)D_{3i}}, \quad \beta_i = \frac{R_{Ei}}{D_{3i}}, \tag{16}$$

for $i = 1, 2$. Constants ξ_i and β_i are small quantities.

In term of the complex amplitudes, the secondary Bjerknes force between bubble 1 and 2, i.e., F_{12}, is given by (see, e.g., [10])

$$F_{12} = 2\pi\rho\omega^2 \frac{R_{E1}^2 R_{E2}^2}{D_{12}^2} \Re(A_1^* A_2). \tag{17}$$

When $\alpha_1 = \alpha_2 = 0$, the system describes the interaction between two bubbles without the interference from the third bubble, since $\alpha_1 = \alpha_2 = 0$ implies the third bubble is infinitely far away from the other two bubbles. The expression for F_{12} in this case is denoted by $F_{12}^{[2]}$. Using Eqs. (12) and (13), the well-known expression for $F_{12}^{[2]}$ is recovered (see, e.g., [32] and [10]):

$$F_{12}^{[2]} = H^{[2]} \left(\omega^2 - \frac{1}{1-\xi_1}\omega_1^2 \right) \left(\omega^2 - \frac{1}{1-\xi_2}\omega_2^2 \right), \tag{18}$$

with the pre-factor $H^{[2]}$ given by

$$H^{[2]} = \frac{2\pi\rho\omega^2 \xi_1 \xi_2 |A_p|^2}{\Delta^2} (1-\xi_2)(1-\xi_1). \tag{19}$$

Without loss of generality, we assume $\omega_1 \leq \omega_2$. The main conclusions drawn from Eq. (18) are as follows:

1. F_{12} is a function of D_{12}. When $\omega_1 \lesssim \omega_2 \lesssim \omega$, a distance $D_{12} \equiv D_E$ exists where $F_{12} = 0$ and F_{12} is an increasing function of D_{12} at the neighborhood of D_E. At D_E, the two bubbles are in a stable equilibrium. The expression for D_E is

$$D_E^{[2]} = \max\left(\frac{R_{E1}\omega^2}{\omega^2 - \omega_1^2}, \frac{R_{E2}\omega^2}{\omega^2 - \omega_2^2} \right). \tag{20}$$

   The two expressions on the right hand side of Eq. (20) are the roots of the last two factors in Eq. (18), respectively.

2. Such an equilibrium distance does not exist when $\omega_1 \lesssim \omega \lesssim \omega_2$ or $\omega \lesssim \omega_1 \lesssim \omega_2$.

As mentioned in Section 1, the existence of $D_E^{[2]}$ qualitatively explains why stable bubble clusters may exist.

In the presence of the third bubble, α_i ($i = 1, 2$) are no longer zero. The force is given by

$$F_{12}^{[3]} = H^{[3]} \left(\omega^2 - f_1\omega_1^2\right)\left(\omega^2 - f_2\omega_2^2\right), \tag{21}$$

with $H^{[3]}$ given by

$$H^{[3]} = \frac{2\pi\rho\omega^2\xi_1\xi_2|A_p|^2(1+\alpha_1)(1+\alpha_2)}{\Delta^2 f_1 f_2}, \tag{22}$$

where

$$f_i = \frac{1+\alpha_{3-i}}{(1+\alpha_{3-i})(1-\xi_i) + (\alpha_i - \alpha_{3-i})\beta_i}. \tag{23}$$

Setting the last two factors on the right hand side of Eq. (21) to zero, we may find two values for D_{12},

$$D_{E1}^{[3]} = \frac{R_{E1}\omega^2(1+\alpha_1)}{\omega^2[1+\alpha_2+(\alpha_1-\alpha_2)\beta_1] - (1+\alpha_2)\omega_1^2}. \tag{24}$$

and

$$D_{E2}^{[3]} = \frac{R_{E2}\omega^2(1+\alpha_2)}{\omega^2[1+\alpha_1+(\alpha_2-\alpha_1)\beta_2] - (1+\alpha_1)\omega_2^2}, \tag{25}$$

$D_{Ei}^{[3]}$ ($i = 1, 2$) represent the distances where $F_{12}^{[3]} = 0$ (as long as they are positive). However, due to the complexity of Eq. (21), it is not trivial to ascertain analytically if $F_{12}^{[3]}$ is increasing with D_{12} at these values. In what follows, we numerically evaluate Eq. (21), Eq. (24) and Eq. (25) to find $D_E^{[3]}$. Note that, for a three bubble system, there are secondary Bjerknes forces between the third bubble and the other two, individually. When $D_{12} = D_E^{[3]}$, $F_{12}^{[3]}$ is zero but in general the other two secondary Bjerknes forces are not. Therefore the total force on bubble 1 and 2 are not necessarily zero and the two bubbles are not actually in equilibrium. Nevertheless, $D_E^{[3]}$ is still a useful quantity to characterize the effects of the third bubble on F_{12}.

Eqs. (24) and (25) show that $D_E^{[3]} = D_E^{[2]}$ when $\alpha_1 = \alpha_2$, which happens when $D_{32} = D_{31}$, i.e., when the third bubble is on the mid-plane between the two bubbles. In general, however, $D_E^{[3]}$ is different from $D_E^{[2]}$. $D_E^{[3]}$ will be calculated from Eqs. (21), (24) and (25), and compared with $D_E^{[2]}$ given in Eq. (20). In the first case to be considered, the bubbles are arranged in a line in the order of $1-2-3$, so that $D_{13} = D_{12} + D_{23}$. The other parameters used in the calculation are given in Table 1. The computed D_E is unphysical if it is too small since one of the premises of the model is that D_{12} should be much larger than the radii of the bubbles. Therefore,

Parameter	Value
ρ	$998\ \mathrm{kg\,m^{-3}}$
σ	$0.0725\ \mathrm{Nm^{-1}}$
c	$1500\mathrm{m\,s^{-1}}$
ν	$1.002\times10^{-6}\ \mathrm{m^2 s^{-1}}$
f	$20\times10^3\mathrm{Hz}$
ω	$2\pi f$
p_0	$1.013\times10^5\mathrm{Pa}$

Table 1: Parameters used in the simulations. ρ: density; σ: surface tension; c: sound speed; ν: kinematic viscosity; f: driving frequency; ω: driving angular frequency; p_0: ambient pressure.

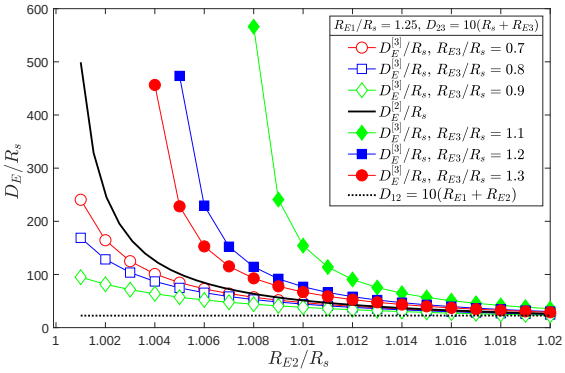

Figure 2: $D_E^{[2]}$ and $D_E^{[3]}$ as functions of R_{E2} for different parameters. $R_s = 164.9\mu$m is the resonant radius corresponding to the driving frequency ω (c.f., Eq. (9)). The bubbles are colinear, in the order of bubble 1, 2, and 3 from left to right, with D_{23} fixed.

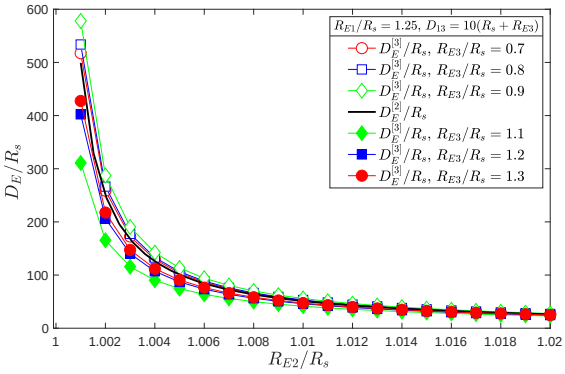

Figure 3: Same as Fig. 2 but the bubbles are aligned in the order of bubble 2, 1, and 3 from left to right, with D_{13} fixed.

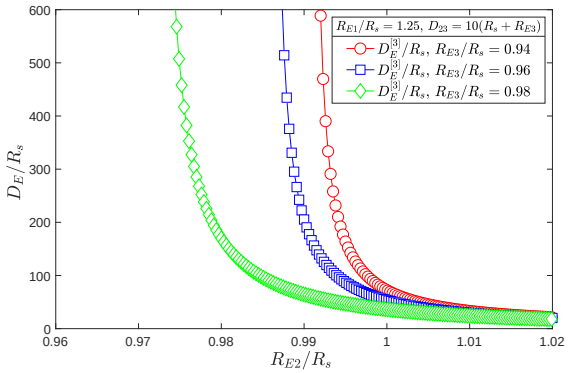

Figure 4: Same as Fig. 2 but for R_{E3}/R_s approaching 1 from below.

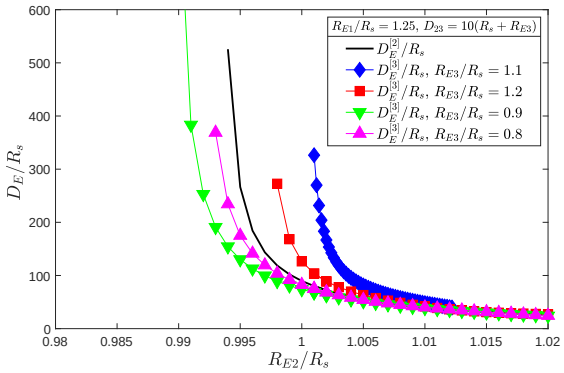

Figure 5: D_E/R_s versus R_{E2}/R_s from the numerical solutions of Eq. (5) for $p_a = 0.01 p_{\rm atm}$.

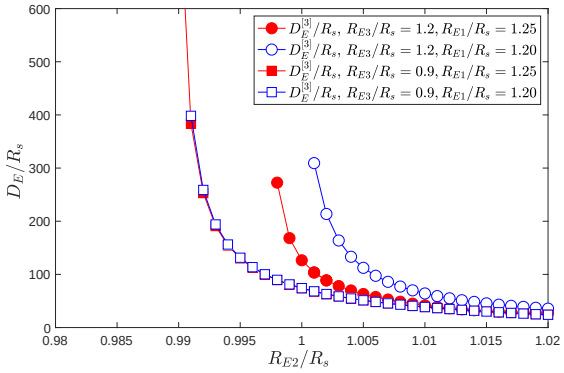

Figure 6: $D_E^{[3]}/R_s$ versus R_{E2}/R_s from the numerical solutions of Eq. (5) for $p_a = 0.01 p_{\rm atm}$, with different R_{E1} and R_{E3} and $D_{23} = 10(R_{E3} + R_{E2})$.

$10(R_{E1} + R_{E2})$ has been chosen as the minimum value of D_{12} for which the model remains physical. The results will be non-dimensionalized by the resonant radius R_s, which is defined implicitly by the following equation:

$$\omega \equiv \left[\frac{3kp_0}{\rho} + \frac{(3k-1)2\sigma}{\rho R_s}\right]^{1/2} \frac{1}{R_s}. \qquad (26)$$

The first set of results are shown in Fig. 2. The main observation is that $D_E^{[3]}$ is reduced by the third bubble when $R_{E3} < R_s$, and increased when $R_{E3} > R_s$. The difference between $D_E^{[3]}$ and $D_E^{[2]}$ are amplified when R_{E3} approaches R_s (from either side of R_s). We also observe that the change in D_E is already negligible when $R_{E3} = 10R_s$ although the curve is not shown.

Fig. 3 plots $D_E^{[3]}$ for three colinear bubbles aligned in the order of bubbles 2, 1 and 3, so that bubble 3 is further away from bubble 2. Although the same parameters as in Fig. 2 are used, only weak effects are produced in this case. Compared with $D_E^{[2]}$, $D_E^{[3]}$ is smaller (larger) for $R_{E3} < R_s$ ($R_{E3} > R_s$), opposite to Fig. 2. On the other hand, although the effects are much weaker, we do observe that the modulation effects are stronger when R_{E3}/R_s is closer to 1, a behavior also observed in Fig. 2.

A particular consequence of having the third bubble is that D_E may exist for $\omega_2 > \omega$, i.e., for $R_{E2} < R_s$, whereas this scenario is not possible for linearly oscillating two bubble systems. This behaviour is illustrated in Fig. 4, which shows that $D_E^{[3]}$ exists for a small range of values for $R_{E2}/R_s < 1$ when R_{E3} is very close to R_s. However, given that the range is small, the observation that these values exist is less important than the observation that $D_E^{[3]}$ is very sensitive to the values of R_{E2} and R_{E3} in this range.

The linear analysis is valid for infinitesimal oscillations and has neglected viscous dissipation. We collaborate the linear analysis with the numerical solutions of Eq. (5), with viscosity included. Small pressure amplitude $p_a = 0.01 p_{\rm atm}$ is chosen since we want to investigate weak oscillations. Only the case where the bubbles are colinearly aligned in the $1-2-3$ configuration is considered. The results are given in Fig. 5. The case with only two bubbles is plotted with the thick solid line, whereas thin lines with symbols are results for three bubble systems with different R_{E3}. For a given R_{E2}, both $D_E^{[2]}$ and $D_E^{[3]}$ obtained here are smaller than those in Fig. 2, in such a way that the curves appear to have shifted to the left. However, the curves are qualitatively the same on two aspects. Firstly, $D_E^{[3]}$ is larger (smaller) than $D_E^{[2]}$ for $R_{E3} > R_s$ ($R_{E3} < R_s$). Secondly, the difference between $D_E^{[2]}$ and $D_E^{[3]}$ is larger when R_{E3}/R_s is closer to 1. Therefore, the numerical solution validates the linear analysis.

Fig. 6 plots the numerical solution for $D_E^{[3]}$ for two different R_{E3} and R_{E1}. $D_E^{[3]}$ sensitively depends on R_{E1} when $R_{E3} > R_s$, and it is increased when R_{E1} approaches R_s. However, it barely changes with R_{E1} when $R_{E3} < R_s$.

The difference between $D_E^{[3]}$ and $D_E^{[2]}$ is a consequence of changes in the oscillatory behaviours of bubbles 1 and 2 induced by the third bubble. $R_i(t)$ $(i = 1, 2, 3)$ is plotted

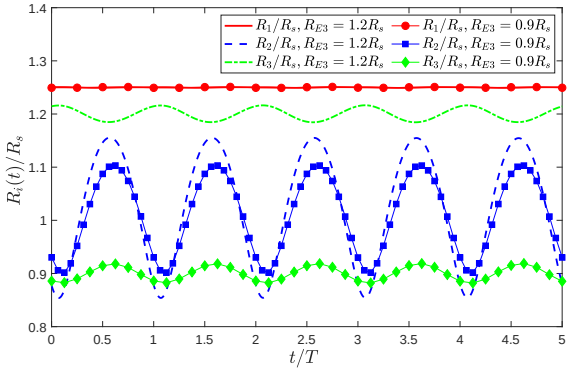

Figure 7: $R_i(t)$ for two different R_{E3}, with $R_{E1} = 1.25R_s$, $R_{E2} = R_s$, $D_{23} = 10(R_{E2} + R_{E3})$, and $p_a = 0.01p_{\rm atm}$. $D_{12} = 100R_s$.

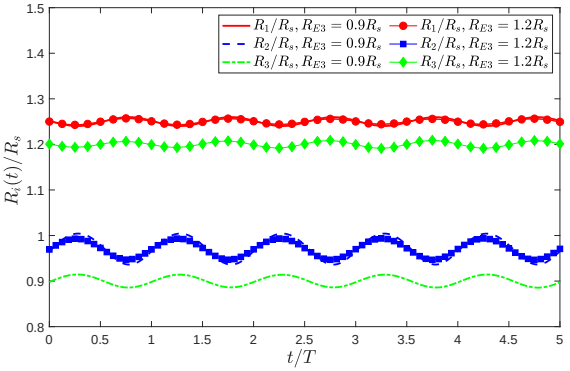

Figure 9: $R_i(t)$ for $R_{E2} = 0.97R_s$. The other parameters as the same as in Fig. 8. The two curves for $R_1(t)/R_s$ fall on each other.

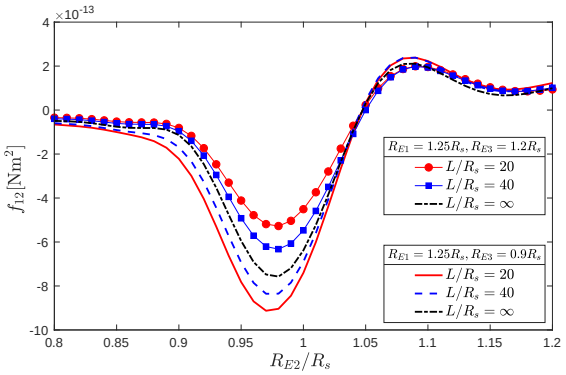

Figure 8: f_{12} as a function of R_{E2} for different L and R_{E3}, with $D_{12} = 20R_s$ ($R_s = 164.9\mu$m), $\theta = 90°$, and $p_a = 0.01p_{\rm atm}$.

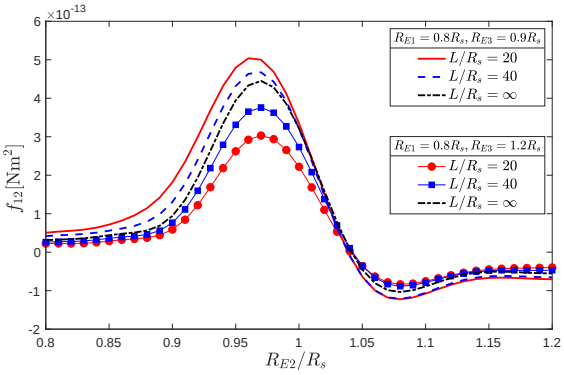

Figure 10: Same as Fig. 8 except for $R_{E1} = 0.8R_s$.

in Fig. 7 for two R_{E3} values with $D_{12} = 100R_s$. $R_2(t)$ and $R_3(t)$ oscillate *in phase* when $R_{E3} = 0.9R_s$. As a result, bubble 3 increases the apparent stiffness of flow field and reduces the amplitude of $R_2(t)$. The amplitude of $R_1(t)$ is slightly enhanced although it is not visible on the curve because the oscillation of $R_1(t)$ is much weaker. The effects increase the secondary Bjerknes force f_{12} between the two bubbles at this distance D_{12}, and lead to decreased $D_E^{[3]}$. The situation for $R_{E3} = 1.2R_s$, however, is the exact opposite because $R_2(t)$ and $R_3(t)$ oscillate *out of phase* in this case, and as a result $D_E^{[3]}$ is increased.

We have only considered the colinear configurations in the above discussion. The calculation can be easily conducted for non-colinear bubbles. The results are not shown here, but qualitatively speaking, they fall between those for the two extreme colinear configurations. This point is also observed in the results for strongly nonlinear oscillations to be discussed in the next section.

Finally, we look into the magnitude of the secondary Bjerknes force f_{12}. The result is shown in Fig. 8 for several distances L and R_{E3} (see Fig. 1 for the definitions for L and θ). In all cases, $R_{E1} = 1.2R_s$. The time sequences $R_i(t)$ for $R_{E2} = 0.97R_s$ are given in Fig. 9 to complement Fig. 8. For these given parameters, Fig. 8 shows that f_{12} is negative (or positive) for $R_{E2}/R_s \lesssim 1.05$ (or $R_{E2}/R_s \gtrsim 1.05$). These happen when R_{E2} and R_{E1} are out of phase and in phase, respectively. Fig. 9 demostrates this for $R_{E2} = 0.97R_s$. The effects of R_{E3} (i.e., the third bubble) is the strongest when $f_{12} < 0$ (with $R_{E2} \approx 0.97R_s$). The curves with different L show that, as expected, the effects of R_{E3} are stronger when L is smaller (so that the third bubble is closer to the other two bubbles). For $R_{E3} = 1.2R_s$, the magnitude of f_{12} is reduced with smaller L, and increased for $R_{E3} = 0.9R_s$. Fig. 9 shows that these effects mainly come from the changes in $R_2(t)/R_s$ induced by R_{E3}, since $R_1(t)$ is almost the same for the two R_{E3}'s. $R_2(t)$ is reduced when $R_{E3} = 1.2R_s$, leading to a f_{12} with a smaller magnitude. The opposite happens when $R_{E3} = 0.9R_s$.

Fig. 10 is the same as Fig. 8 except for $R_{E1} = 0.8R_s$ (instead of $1.2R_s$). As R_{E1} is now smaller than R_s, f_{12} is now positive when $R_{E2}/R_s \lesssim 1.05$. Fig. 11 shows that the amplitude of $R_2(t)$ again is suppressed when $R_{E3} =$

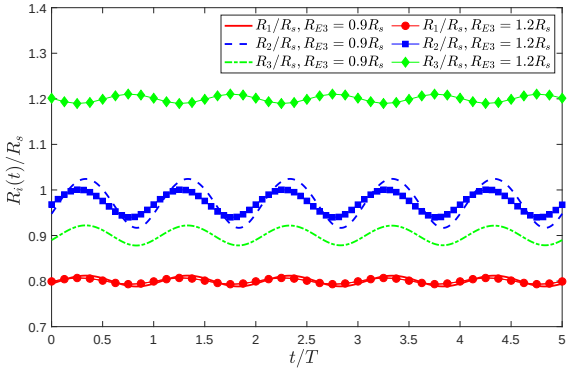

Figure 11: $R_i(t)$ for $R_{E2} = 0.97R_s$. The other parameters are the same as in Fig. 10.

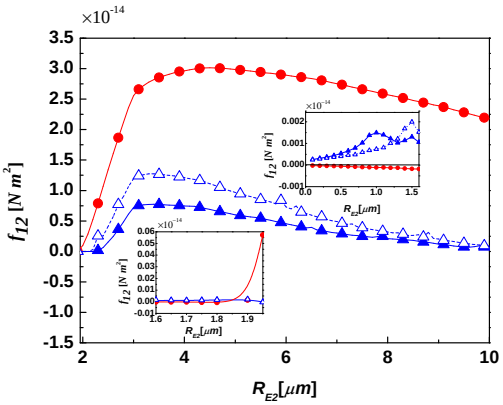

Figure 12: f_{12} as a function of R_{E2} for $L = 100\mu$m (filled triangles), 200μm (empty triangles), and ∞ (circles) with $R_{E1} = 3\mu$m, $R_{E3} = 5\mu$m, $D = 100\mu$m, $\theta = 90°$, $p_a = 1.32p_{\rm atm}$, and $f = 20$kHz.

$1.2R_s$. This effect leads to reduced f_{12} as is shown in Fig. 10. Again, the opposite is observed for $R_{E3} = 0.9R_s$.

4. The analysis of strongly nonlinear oscillations

For large driving pressure amplitude p_a, transient cavitation occurs and the oscillations of the bubbles are highly anharmonic. The features of the secondary Bjerknes force in this case are investigated numerically and are presented in this subsection. The parameter values in Table 1 are used. $p_a = 1.32p_{\rm atm}$ is chosen because it is known that this value induces transient cavitation for the given parameters. At high p_a, the response curve (see e.g. [19]) shows that transient cavitation is the strongest for small bubbles with radii just slightly above the dynamic Blake threshold. Therefore, bubbles with radii of the order of a few microns have been considered. For strong oscillations, the resonant radius R_s is not the relevant characteristic radius. For this reason, the results have not been non-dimensionalized, which is also the tradition in the literature. The unit of the lengths is always μm unless stated otherwise. L and θ, as defined in Fig. 1, are used to define the relative locations of the bubbles.

Fig. 12 shows the general feature of f_{12} as a function of R_{E2} for a given R_{E1} and several R_{E3}. The peaks of the curves are found around $R_{E2} \approx R_{E1}$. The magnitude of f_{12} is reduced when L is decreased, i.e., when the third bubble is moved closer to the bubble pair. Presumably, the reduction is caused by the third bubble increasing the apparent stiffness for the two bubbles, since the bubbles mostly oscillate in phase during the transient expansion stage. Comparing Fig. 12 with Figs. 8 and 10, one observes that f_{12} appears to be smaller in the strong nonlinear oscillation regime. However, we note that the radii of the bubbles in Figs. 8 and 10 are much larger, at the order of 100μm. Therefore the secondary Bjerknes force is actually much stronger in the nonlinear oscillation regime

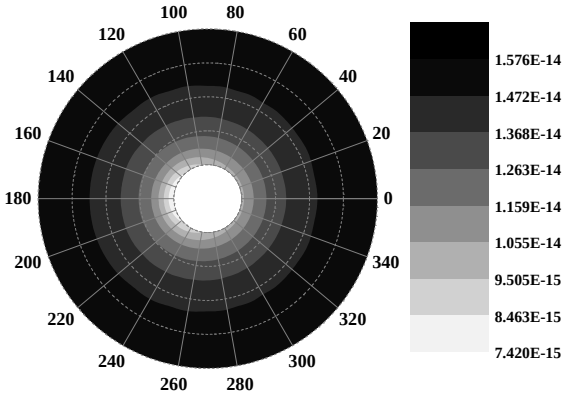

Figure 13: f_{12}[Nm^2] as a function of L and θ for $(R_{E1}, R_{E2}) = (3, 5)\mu$m with $D = 100\mu$m, $R_{E3} = 5\mu$m, $p_a = 1.32p_{\rm atm}$, and $f = 20$kHz. The radii of the circles shown with dashed lines increase from 200μm to 1000μm with an increment equal 200μm.

when the radii of the bubbles and other parameters are similar.

Figs. 13 to 15 plot f_{12} as a function of θ and L for three different R_{E2} values. The figures show that the force increases with L and that the effect of the third bubble is weaker when L is larger, consistent with Fig. 12. In addition, the values at different angles show that f_{12} is reduced more when the third bubble is place on the side of the smaller bubble in the bubble pair. This observation is confirmed by Fig. 16, which extracts the f_{12} values at $L = 200\mu$m from Fig. 13 to 15 and plots them against θ. The magnitude of f_{12} is the largest when $R_{E2} = 3\mu$m, which has been shown in Fig. 12. For $(R_{E1}, R_{E2}) = (3\mu$m, 5μm), stronger reduction is found at $\theta = 180°$, while for $(R_{E1}, R_{E2}) = (3\mu$m, 2.5μm), stronger reduction is found at $\theta = 0°$. That is, stronger reduction is found when the third bubble is on the side of the

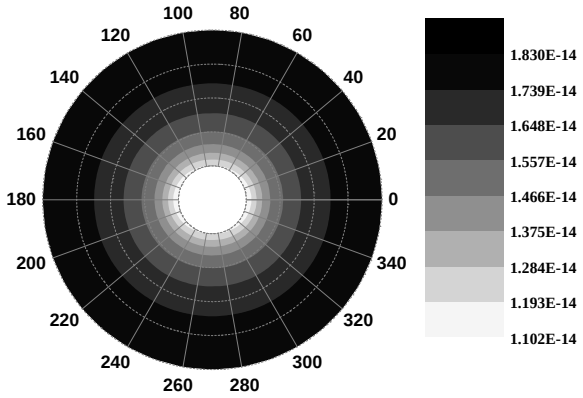

Figure 14: Same as Fig. 13 except that $R_{E2} = 3\mu$m.

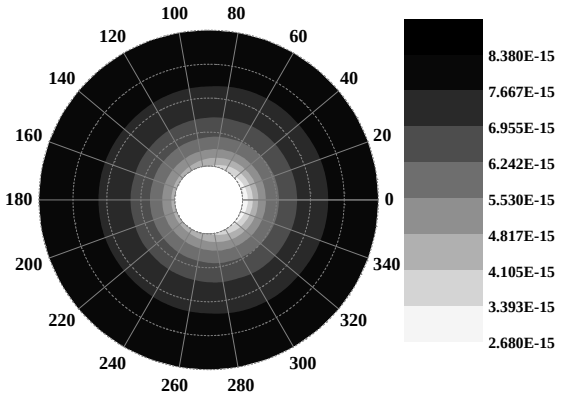

Figure 15: Same as Fig. 13 except that $R_{E2} = 2.5\mu$m.

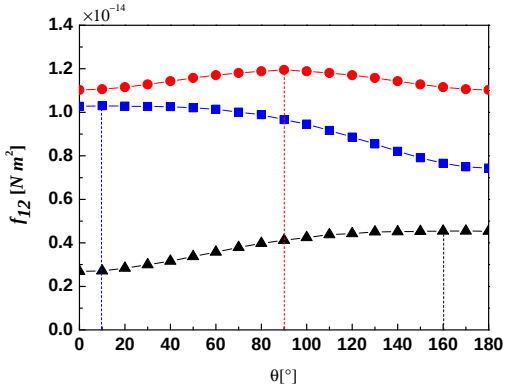

Figure 16: f_{12} as a function of θ for $R_{E2} = 2.5\mu$m (filled triangles), 5μm (squares) , and 3μm (circles) with $R_{E1} = 3\mu$m, $R_{E3} = 5\mu$m, $D = 100\mu$m, $L = 200\mu$m, $p_a = 1.32p_{\text{atm}}$, and $f = 20$kHz.

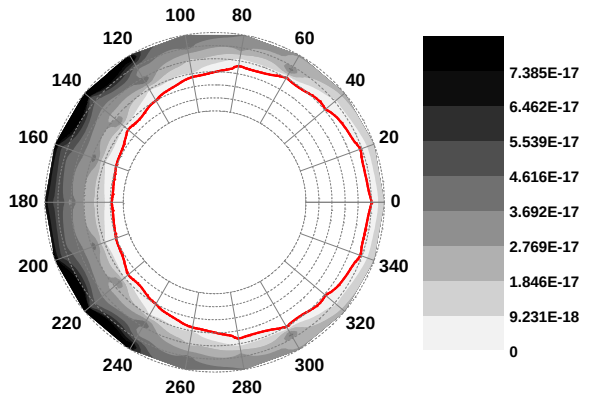

Figure 17: f_{12}[Nm^2] as a function of L and θ for $(R_{E1}, R_{E2}) = (3.5\mu\text{m}, 2.1\mu\text{m})$ with $D = 100\mu$m, $R_{E3} = 5\mu$m, $p_a = 1.32p_{\text{atm}}$, and $f = 20$kHz. The radii of the circles shown with dashed lines increase from 350μm to 650μm with an increment of 50μm. The thick red line shows the distances L where $f_{12} = 0$.

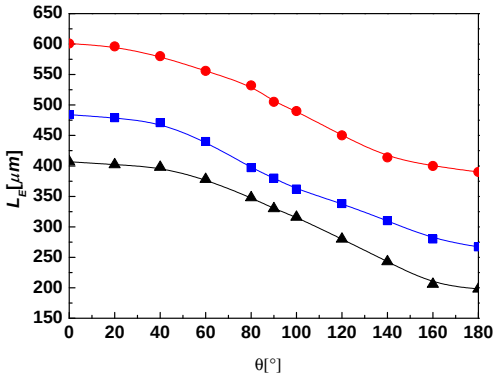

Figure 18: Equilibrium distance L_E as a function of θ with $(R_{E1}, R_{E2}) = (3.3\mu\text{m}, 2.1\mu\text{m})$ (triangles), $(3.4\mu\text{m}, 2.1\mu\text{m})$ (squares), $(3.5\mu\text{m}, 2.1\mu\text{m})$ (circles). $D = 100\mu$m, $R_{E3} = 5\mu$m, $p_a = 1.32p_{\text{atm}}$, and $f = 20$kHz.

smaller bubble.

The cases where $f_{12} = 0$ is of special interests because it is related to the balance between the two bubbles. Some of these cases are documented in Figs. 17 and 18. Fig. 17 plots the contours of f_{12} as a function of θ and L for $(R_{E1}, R_{E2}) = (3.5\mu\text{m}, 2.1\mu\text{m})$. Note that the top and bottom halves of the contours are symmetrical. For a fixed L, f_{12} increases with θ for $0^\circ \le \theta \le 180^\circ$. In other words, the effects of the third bubble are weaker when it is further way from the smaller bubble (bubble 2 in this case). Due to the third bubble, f_{12} becomes negative for a range of L values. The L values where $f_{12} = 0$, referred to as L_E, are marked by the red solid line. The minimum $L_E \approx 400\mu$m is found at $\theta = 180^\circ$, whereas the maximum $L_E \approx 600\mu$m is found at $\theta = 0^\circ$. Therefore, significant effects of the third bubble can be observed even for L as large as $100R_{E3}$.

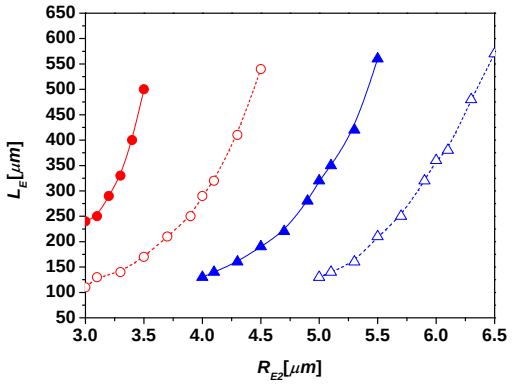

Figure 19: Equilibrium distance L_E as a function of R_{E2} with R_{E1} = 2.1μm (filled circles), 2.2μm (empty circles), 2.3μm (filled triangles), and 2.4μm (empty triangles). D = 100μm, R_{E3} = 5μm, θ = 90°, $p_a = 1.32 p_{\text{atm}}$, and f = 20kHz.

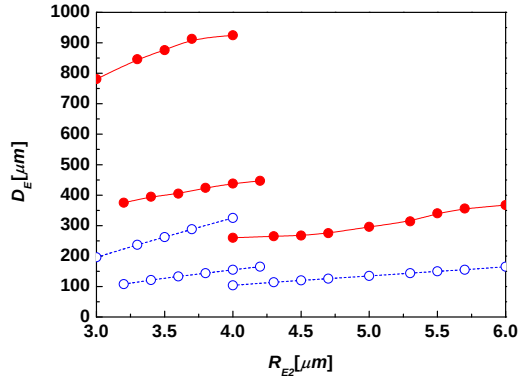

Figure 20: Equilibrium distance D_E as a function of R_{E2} with L = 100μm (filled circles) and $L = \infty$ (empty circles) for R_{E1} = 1.9μm (top), 2.0μm (middle), and 2.1μm (bottom). R_{E3} = 5μm, θ = 90°, $p_a = 1.32 p_{\text{atm}}$ and f = 20kHz.

L_E as a function of θ for several R_{E1} values and R_{E2} = 2.1μm is given in Fig. 18. As expected, the figure shows that L_E decreases with θ for $0° \le \theta \le 180°$. In addition, L_E increases with R_{E1} for the R_{E1} values used in the figure. L_E is plotted as a function of R_{E2} in Fig. 19 for several R_{E1} values which are rather close. For a fixed R_{E1}, L_E increases with R_{E2}. The behaviours in both figures are explained by the fact that f_{12} decreases when the difference between R_{E1} and R_{E2} increases.

The equilibrium distance D_E for D_{12} is plotted in Fig. 20 as a function of R_{E2} for different R_{E1}, L = 100μm and θ = 90°. The figure shows that D_E is increased significantly by the third bubble. This behavior is in contrast to what is observed for weak oscillations, where Eqs. (24) and (25) show that D_E is not changed by the third bubble when θ = 90°. Meanwhile, the dependence on R_{E2} is the same with or without the third bubble, where D_E

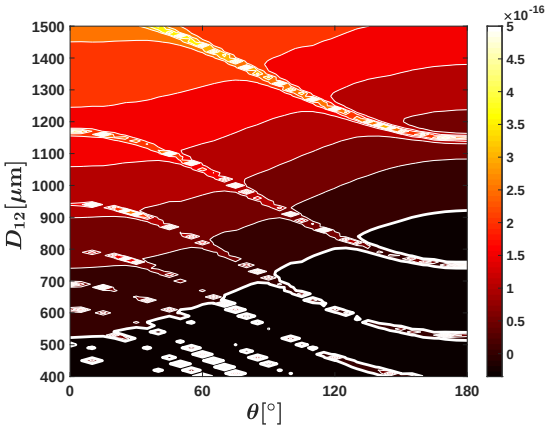

Figure 21: The contour plot of f_{12}[Nm^2] as a function of θ and D_{12} for L = 100μm, R_{E1} = 1.9μm, R_{E2} = 3μm, and R_{E3} = 4μm. Thick contour in white corresponds to f_{12} = 0.

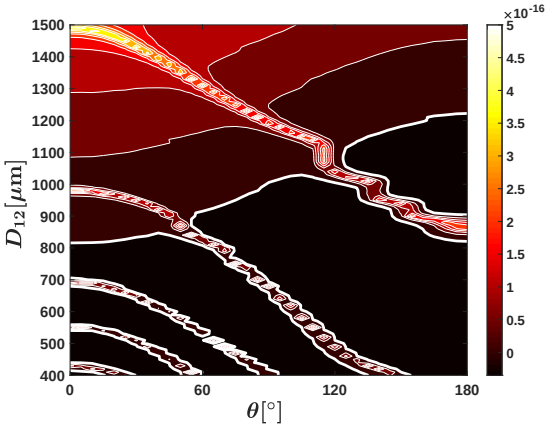

Figure 22: Same as Fig. 21 except that R_{E3} = 6μm.

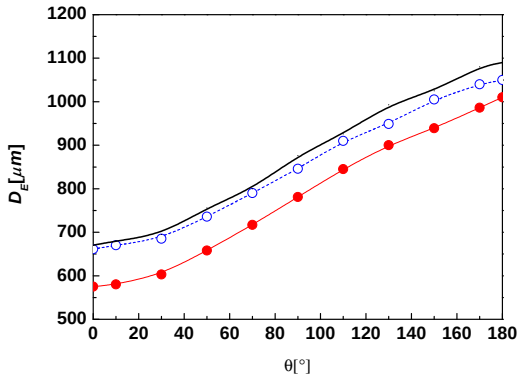

Figure 23: Equilibrium distance D_E as a function of θ for R_{E1} = 1.9μm and R_{E2} = 3μm (filled circles), 3.3μm (empty circles), and 3.5μm (solid line), with L = 100μm, R_{E3} = 5μm, $p_a = 1.32 p_{\text{atm}}$, and f = 20kHz.

increases with R_{E2} gently for the given parameters.

The dependence of D_E on θ, R_{E3} and R_{E2} is examined in the next a few figures. Figs. 21 and 22 plot the contours of f_{12} as a function of θ and D_{12} for $R_{E3} = 4\mu$m and 6μm, respectively. The contour for $f_{12} = 0$, which delineates D_E as a function of θ, is highlighted with a thick white line. A general feature of the figures is that f_{12} is negative for small D_{12} and increases with D_{12}. Small 'islands' of closed contours are observed, which correspond to sharp peaks in the distribution of f_{12}. These peaks are organized in bands, which protrude into areas where f_{12} is otherwise negative. This interesting observation suggests that a resonance-like behavior happens at certain parameter values. Nevertheless, apart from the interruption by these bands, the zero contour shows that D_E increases with θ, i.e., when bubble 3 is positioned relatively closer to the smaller bubble (bubble 1). The comparison between Fig. 21 and 22 shows that f_{12} is smaller for $R_{E3} = 6\mu$m and correspondingly D_E is larger. This behavior again may be explained by the observation that f_{12} generally is smaller when the differences between the radii are increased.

Fig. 23 presents D_E as a function of θ at $R_{E3} = 5\mu$m for several R_{E2}. These curves are of the same nature as the zero contours in Fig. 21 and 22, but we have ignored the interruption by the peaks to highlight the general features. For a given θ, D_E increases with R_{E2} as the latter increases from 3 to 3.5μm. Larger R_{E2}'s are closer to R_{E3} but further away from R_{E1}. The combined effect is to increase D_E in this case. D_E is again larger for larger θ, a trend that has been observed in Fig. 21 and 22.

5. Conclusions

The modulation of the secondary Bjerknes force between a pair of bubbles by a third bubble has been investigated theoretically and numerically. In the linear or weakly nonlinear regime, the characteristic length scale is the resonant radius. Significant modulation effects can be observed when at least one of the two bubbles is approximately in resonance. The third bubble can suppress or increase the secondary Bjerknes force between the bubble pair depending on the Minnaert frequencies of the bubbles. When the third bubble oscillates in (or out of) phase with the nearby bubble, the equilibrium distance is decreased (or increased).

In the strongly nonlinear regime where transient cavitation occurs, small bubbles with radii at the order of a few microns are investigated. The behavior of the modulation can largely be explained by the observation that the secondary Bjerknes force is stronger when the radii of the two bubbles are close. The third bubble reduces the secondary Bjerknes force between the bubble pair and increases the equilibrium distance. Strong effects are observed for a wide range of distances. The effects of the third bubble are stronger when it is placed closer to the smaller one in the pair. Interesting resonance-like behaviours are observed for specific combinations of parameter values.

This investigation has several limitations. In addition to those mentioned in the main text, the bubbles are assumed to be spherical so that the analysis is valid only for small bubbles or weak oscillations. Also, the coupling between bubble translation and oscillation has not been considered. Nevertheless, it demonstrates that the inter-bubble interactions can be significantly modulated by the surrounding bubbles. An implication is that, to model bubble clusters using particle methods, an improved parametrization of the secondary Bjerknes force might be required. A realistic parametrization may need to include as parameters the pressure amplitude, the driving frequency, the relative distances between the bubbles, and the sizes/locations of the bubbles. This question is under investigation and the results will be reported in the future.

6. Acknowledgement

The authors gratefully acknowledge the support provided by the Guangdong provincial Science (Technology) Research Project (Project No. 2015A010105026) and the Guangzhou Science (Technology) Research Project (Project No. 201704030010).

[1] Ahmed, D., Lu, M., Nourhani, A., Lammert, P. E., Stratton, Z., Muddana, H. S., Crespi, V. H., Huang, T. J., 2015. Selectively manipulable acoustic-powered microswimmers. Scientific Reports 5, 9744.

[2] Barbat, T., Ashgriz, N., Liu, C.-S., 1999. Dynamics of two interacting bubbles in an acoustic field. J. Fluid Mech. 389, 137–168.

[3] Bermudez-Aguirre, D., Mobbs, T., Barbosa-Canovas, G. V., 2011. Ultrasound applications in food processing. In: Feng, H., Barbosa-Cánovas, G. V., Weiss, J. (Eds.), Ultrasound Technologies for food and Bioprocessing. Springer, p. 65.

[4] Bjerknes, V. F. K., 1906. Fields of Force. Columbia University press, New York.

[5] Brennen, C. E., 1995. Cavitation and bubble dynamics. Oxford University Press.

[6] Brujan, E. A., 2011. Cavitation in Non-Newtonian Fluids. Springer-Verlag Berlin Heidelberg.

[7] Chen, H., Lai, Z., Chen, Z., Li, Y., 2019. The secondary bjerknes force between two oscillating bubbles in kelvin- voigt-type viscoelastic fluids driven by harmonic ultrasonic pressure. Ultrasonics - Sonochemistry 52, 344–352.

[8] Crum, L. A., 1975. Bjerknes forces on bubbles in a stationary sound field. The Journal of the Acoustical Society of America 57, 1363.

[9] D'Agostino, L., Brennen, C. E., 1989. Linearized dynamics of spherical bubble clouds. J. Fluid Mech. 199, 155–176.

[10] Doinikov, A. A., 1999. Effects of the second harmonic on the secondary bjerknes force. Phys. Rev. E 59, 3016–3021.

[11] Doinikov, A. A., Manasseh, R., Ooi, A., 2005. Time delays in coupled multibubble systems. The Journal of the Acoustical Society of America 117, 47.

[12] Doinikov, A. A., Zavtrak, S. T., 1995. On the mutual interaction of two gas bubbles in a sound field. Phys. Fluids 7, 1923.

[13] Eskin, G. I., Eskin, D. G., 2015. Ultrasonic treatment of light alloy metals. CRC Press.
[14] Harkin, A., Kaper, T. J., Nadim, A., 2001. Coupled pulsation and translation of two gas bubbles in a liquid. J. Fluid Mech. 445, 377–411.
[15] Ida, M., 2009. Multibubble cavitation inception. Phys. Fluids 21, 113302.
[16] Jiao, J., He, Y., Kentish, S. E., Ashokkumar, M., Manasseh, R., Lee, J., 2015. Experimental and theoretical analysis of secondary bjerknes forces between two bubbles in a standing wave. Ultrasonics 58, 35–42.
[17] Keller, J. B., Miksis, M., 1980. Bubble oscillations of large amplitude. J. Acoust. Soc. Am. 68, 628–633.
[18] Lanoy, M., Derec, C., Tourin, A., Leroy, V., 2015. Manipulating bubbles with secondary bjerknes forces. Appl. Phys. Lett. 107, 214101.
[19] Lauterborn, W., Kurz, T., 2010. Physics of bubble oscillations. Rep. Prog. Phys. 73, 106501.
[20] Leighton, T. G., 1994. The Acoustic Bubble. Academic Press, London.
[21] Maeda, K., Colonius, T., 2019. Bubble cloud dynamics in an ultrasound field. J. Fluid Mech. 862, 1105–1134.
[22] Mettin, R., 2005. Bubble structures in acoustic cavitation. In: Doinikov, A. (Ed.), Bubble and Particle Dynamics in Acoustic Fields: Modern Trends and Applications. Kerala, India: Research Signpost, pp. 1–36.
[23] Mettin, R., Akhatov, I., Parlitz, U., Ohl, C. D., Lauterborn, W., 1997. Bjerknes forces between small cavitation bubbles in a strong acoustic field. Phys. Rev. E 56, 2925.
[24] Mettin, R., Luther, S., Ohl, C.-D., Lauterborn, W., 1999. Acoustic cavitation structures and simulations by a particle model. Ultrasonics Sonochemistry 6, 25–29.
[25] Nasibullaeva, E. S., Akhatov, I. S., 2013. Bubble cluster dynamics in an acoustic field. The Journal of the Acoustical Society of America 133, 3727.
[26] Parlitze, U., Mettin, R., Luther, S., Akhatov, I., Voss, M., Lauterborn, W., 1999. Spatio-temporal dynamics of acoustic cavitation bubble clouds. Phil. Trans. R. Soc. Lond. A 357, 313–334.
[27] Pelekasis, N. A., Gaki, A., Doinikov, A., Tsamopoulos, J. A., 2004. Secondary bjerknes forces between two bubbles and the phenomenon of acoustic streamers. J. Fluid Mech. 500, 313–347.
[28] Pelekasis, N. A., Tsamopoulos, J. A., 1993. Bjerknes forces between two bubbles. part 1. response to a step change in pressure. J. Fluid Mech. 254, 467–499.
[29] Pelekasis, N. A., Tsamopoulos, J. A., 1993. Bjerknes forces between two bubbles. part 2. response to an oscillatory pressure field. J. Fluid Mech. 254, 501–527.
[30] Roberts, W. W., 2014. Development and translation of histotripsy: current status and future directions. Curr. Opin. Urol. 24, 104–110.
[31] Yoshida, K., Fujikawa, T., Watanabe, Y., 2011. Experimental investigation on reversal of secondary bjerknes force between two bubbles in ultrasonic standing wave. The Journal of the Acoustical Society of America 130, 135.
[32] Zabolotskaya, 1984. Interaction of gas bubbles in a sound field. Sov. Phys. Acousti. 30, 365.
[33] Zhang, Y., Zhang, Y., Li, S., 2016. The secondary bjerknes force between two gas bubbles under dual-frequency acoustic excitation. Ultrasonics Sonochemistry 29, 129–145.